Feasibility of MRI guided proton therapy: magnetic field dose effects

IOP PUBLISHING PHYSICS IN MEDICINE AND BIOLOGY

Phys. Med. Biol. **53** (2008) 5615–5622 doi:10.1088/0031-9155/53/20/003

Feasibility of MRI guided proton therapy: magnetic field dose effects

B W Raaymakers, A J E Raaijmakers and J J W Lagendijk

Department of Radiotherapy, University Medical Center Utrecht, Heidelberglaan 100, 3584 CX, Utrecht, The Netherlands

E-mail: B.W.Raaymakers@umcutrecht.nl

Received 18 April 2008, in final form 7 July 2008
Published 17 September 2008
Online at stacks.iop.org/PMB/53/5615

Abstract

Many methods exist to improve treatment outcome in radiotherapy. Two of these are image-guided radiotherapy (IGRT) and proton therapy. IGRT aims at a more precise delivery of the radiation, while proton therapy is able to achieve more conformal dose distributions. In order to maximally exploit the sharp dose gradients from proton therapy it has to be combined with soft-tissue based IGRT. MRI-guided photon therapy (currently under development) offers unequalled soft-tissue contrast and real-time image guidance. A hybrid MRI proton therapy system would combine these advantages with the advantageous dose steering capacity of proton therapy. This paper addresses a first technical feasibility issue of this concept, namely the impact of a 0.5 T magnetic field on the dose distribution from a 90 MeV proton beam. In contrast to photon therapy, for MR-guided proton therapy the impact of the magnetic field on the dose distribution is very small. At tissue–air interfaces no effect of the magnetic field on the dose distribution can be detected. This is due to the low-energy of the secondary electrons released by the heavy protons.

(Some figures in this article are in colour only in the electronic version)

1. Introduction

The challenge of modern radiotherapy is to escalate the dose to the tumour while minimizing the dose to the surrounding organs at risk. In the field of radiotherapy physics there are two large research areas which aim to achieve this goal: (1) image-guided radiotherapy (IGRT), improving the accuracy of dose delivery (see, for instance, (Dawson and Sharpe 2006)) and (2) intensity modulated radiotherapy (IMRT) (Webb 2001) using either photons or protons in order to improve the conformality of the dose distribution to the tumour shape.

MRI offers unequalled soft-tissue contrast and is therefore a favourable candidate for image guidance in radiotherapy. Recently we showed the technical feasibility of a hybrid

1.5 T MRI and a 6 MV photon therapy system for real-time IGRT (Raaymakers *et al* 2004a, Lagendijk *et al* 2008). A prototype of this system is currently under construction.

For IMRT, the physics of proton therapy (Schulz-Ertner *et al* 2006) is favourable for creating highly conformal dose distributions. In particular, small tumours and tumours very close to critical organs can benefit from proton therapy, see Greco and Wolden (2007) for a recent review. A drawback of proton therapy is its sensitivity for range variations by changes in the anatomy between planning and delivery (Lomax 2008). A solution is to take the expected anatomy variations into account during treatment planning and make the dose distribution less sensitive for range variations (Unkelbach *et al* 2007). However, to maximally exploit the high dose gradients of proton therapy IGRT is necessary in order to control anatomy variations relative to the treatment planning.

In general, IGRT is the first step towards optimizing radiotherapy. IGRT decreases the geometric uncertainties during radiation delivery and therefore the margins around the tumour to account for these uncertainties can be reduced. Then as a second step the conformality of the dose distribution can be optimized, as can be done by proton therapy. It is a waste of effort to create a very conformal dose distribution when the target volume still consists for a large part of healthy tissue. Additionally, as mentioned above, proton therapy is particularly advantageous for small target volumes. Given this importance of IGRT in general and the sensitivity for anatomy variations for proton therapy, proton therapy can benefit greatly from MRI guidance.

Clearly, the integration of a proton therapy facility with on-line MRI functionality faces several technical hurdles. These are briefly discussed in section 4.2. A full assessment of the technical feasibility is beyond the scope of this paper. The advent of compact proton accelerators such as presented by the Tomotherapy company (see news release NR-07-06-06[1] from Lawrence Livermore National Laboratory) and an open 0.5 T MRI similar to the hybrid interventional MR/X-ray system by Fahrig *et al* (2001) initiate the thoughts on a hybrid MRI proton therapy system. Also from an economical point of view this seems justified: the additional investment for MRI guidance is small compared to the total investment for a proton therapy facility.

A major issue for the hybrid MRI photon therapy system is the impact of the magnetic field on the dose distribution (Raaymakers *et al* 2004b). Particularly at tissue–air interfaces a large dose increase occurs due to returning electrons, the so-called Electron Return Effect (ERE) (Raaijmakers *et al* 2005, 2007b, 2008). Raaijmakers *et al* (2007a) showed that proper beam configuration in combination with IMRT can fully compensate for these magnetic field induced dose effects. This paper addresses the magnetic field dose effects for proton irradiation in the presence of a 0.5 T magnetic field. 0.5 T was chosen because the current open MRI systems are limited in field strength at 0.5 T due to mechanical stability. Although an open 3.0 T MRI system is not technically feasible at the moment, 3.0 T was investigated to complete the picture of the impact of the magnetic field on the dose distribution in proton therapy.

2. Methods

Monte Carlo simulations using Geant4, version 9.0, (Agostinelli 2003, Allison 2006) are used to investigate the impact of a 0.5 T magnetic field on the dose deposition for proton therapy.

For photons, electrons and positrons, the low-energy EM-physics package has been used. For hadrons (including protons) and ions, EM-physics processes multiple scattering and low-energy ionization have been used, along with decay, elastic and inelastic physics processes.

[1] https://publicaffairs.llnl.gov/news/news_releases/2007/NR-07-06-06.html.

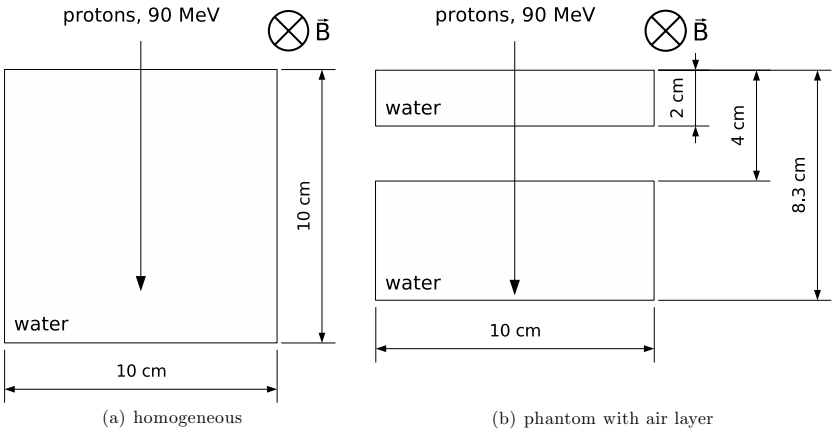

(a) homogeneous (b) phantom with air layer

Figure 1. Simulation setup for the calculation of proton dose distribution in the presence of a magnetic field in a homogeneous water phantom (a) and a water phantom with an air layer (b). Note that that in situation (b) the Bragg peak is located at the distal water–air interface.

The secondary electrons in proton therapy have very low energies. For reliable simulations and more complete energy spectra, the cutValue was set to 0.001 mm. For both water and air, this cutValue corresponds to an energy value that is lower than the internal minimum particle energy of 250 eV. For the calculation of the tracks of charged particles in the magnetic field, the default method, i.e. Runge–Kutta, was used.

The proton dose deposition in the presence of a magnetic field was studied for two geometries.

First, the dose deposition in a homogeneous medium is simulated. A pencil beam of 10 000 mono-energetic 90 MeV protons is fired at a $10 \times 10 \times 10$ cm^3 water phantom; see figure 1(a). The water phantom is covered with a $1 \times 5 \times 1$ mm^3 dose scoring grid. After this simulation, the dose distribution of a 5×5 cm^2 beam is obtained by convolution of the pencil beam kernel. The statistic uncertainty of the dose distribution is below 1.6%.

Second, the dose distribution in an inhomogeneous medium is simulated. Again, a pencil beam of 10 000 mono-energetic 90 MeV protons is fired at a water phantom. Before arriving at the Bragg peak, the protons pass through an air layer of 2 cm thickness. The dimensions of the phantom are now $10 \times 10 \times 8.3$ cm^3, resulting in the Bragg peak being located exactly at the water–air interface at the distal side of the phantom (see figure 1(b)). Also here, the statistic uncertainty of the dose distribution is below 1.6%.

All simulations were carried out at 0, 0.5 and at 3.0 T.

Additionally, we pursued more insight in the energy characteristics of the protons and secondary electrons. Therefore, the energy spectrum of the protons and secondary electrons have been determined as a function of the depth in the homogeneous phantom. Again this was done at 0, 0.5 and 3.0 T.

3. Results

3.1. Dose distributions

The average energy of the protons as a function of the depth is shown in figure 2 for 0 and 0.5 T. The graphs are the same, also the case for 3 T (not presented) shows exactly the

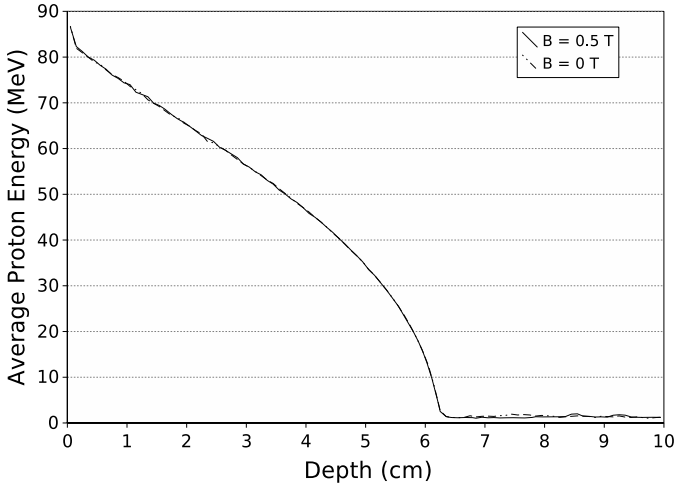

Figure 2. The average proton energy versus depth in a homogeneous water phantom for a 90 MeV proton pencil beam for $B = 0$ T and $B = 0.5$ T . Note that the lines are perfectly overlapping.

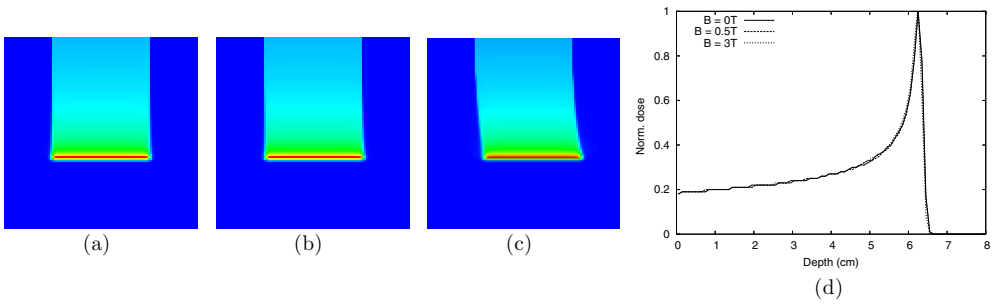

Figure 3. The dose distribution in a homogeneous water phantom for $B = 0$ T (a), 0.5 T (b) and 3.0 T (c) and the central depth dose profiles through the dose distributions (d). Note that there are actually three overlapping lines in (d).

same graph. The average energy of the protons starts at 90 MeV, gradually decreases until it decreases very rapidly at the Bragg peak depth. The average energy as a function of depth does not depend on the magnetic field strength.

The dose distribution of a 5×5 cm^2 proton beam has been determined by convolution. This distribution is shown in figure 3. The Bragg peak is clearly visible around 6 cm depth. Except for the shift of the field by 1 mm at the Bragg peak, caused by the proton beam curvature, no difference can be detected between the case of 0 and 0.5 T. For 3.0 T the profile is again the same, except that the lateral shift is now 5 mm.

In figure 4 the dose distribution for the layered, water–air–water phantom is shown for 0, 0.5 and 3.0 T magnetic field. Again, the Bragg peak is clearly visible. At 0.5 T, the lateral dose shift due to the proton beam curvature is the same as in the homogeneous case, i.e. 1 mm at the Bragg peak. For 3.0 T the lateral shift of the Bragg peak is 8 mm. No impact of the magnetic field can be seen at any of the tissue–air interfaces.

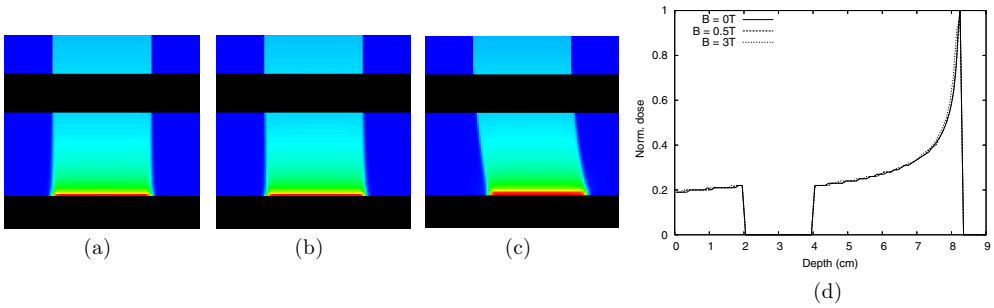

Figure 4. The dose distribution in a water phantom with an air gap for $B = 0$ T (a), 0.5 T (b) and 3.0 T (c) and the central depth dose profiles through both dose distributions (d). Note that there are actually three overlapping lines in (d).

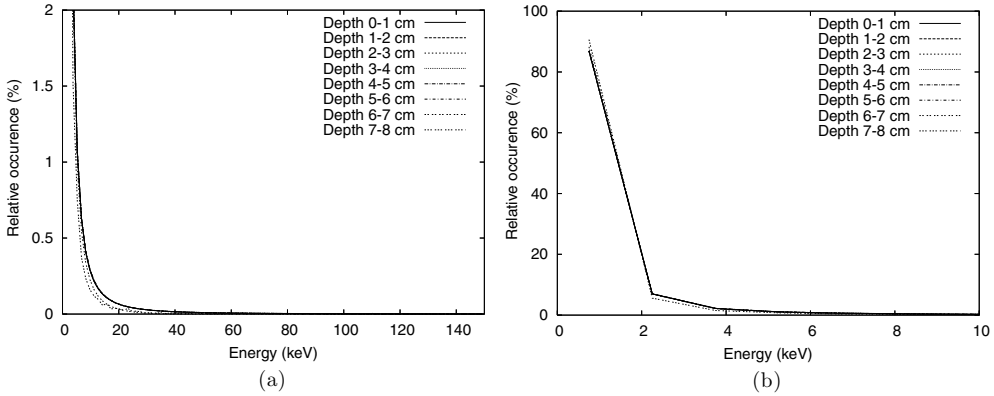

Figure 5. The energy histograms for secondary electrons at various depths. Note the scale on the *Y*-axis in (a). Figure 5(b) is a zoom in on the low-energy part of figure 5(a). The lines for various depths are overlapping.

3.2. Energy spectra of secondary electrons

For the 0 T case, figure 5 shows that the energy histograms for the secondary electrons are not dependent on the depth.

Figure 5(b) also shows that the vast majority of electrons have an energy below 2 keV. The average electron energy is approximately 1.5 keV. The results for the 0.5 and the 3.0 T case (both not presented) are similar to the 0 T case.

4. Discussion

4.1. Impact magnetic field on dose distribution

The impact of a 0.5 or a 3.0 T magnetic field on the dose distribution from a 90 MeV proton beam is limited to the proton beam curvature in the magnetic field. For 0.5 T the curvature of a 90 MeV proton beam in a vacuum is 2.8 m. Over a depth of 6 cm, this would correspond to a lateral displacement of 0.2 mm. However, the average energy of the protons decreases (figure 2). Therefore the curvature decreases with increasing depth, resulting in a 1 mm lateral

displacement. Note that irradiations for larger depths will use higher energies that have even larger (initial) curvatures. It is safe to say that for 0.5 T and the dimensions of a human body, the lateral shift of the Bragg peak will remain well below 2 mm for any practical proton energy and is completely predictable. For 3.0 T the curvature of the proton beam is more pronounced. The lateral shift of the Bragg peak increases with increasing penetration depth, as can be seen when comparing the lateral shift in figures 3(c) and 4(c). The 2 cm wide air gap causes a longer proton beam track and thus a larger lateral shift.

Strikingly different from irradiation with photons in the presence of a magnetic field is the absence of the electron return effect: at tissue–air interfaces large dose increase is shown for the case with magnetic field due to returning electrons (Raaijmakers *et al* 2008, Kirkby *et al* 2008). This difference can be attributed to the difference in the energies of the secondary electrons. Raaijmakers *et al* (2008) show that for a 6 MV photon beam the average secondary electron energy is approximately 1 MeV. This is almost three orders of magnitude higher than the 1.5 keV for the average secondary electron energy in a 90 MeV proton beam (see figure 5). The very heavy protons release only very low energy electrons. This follows from the laws of conservation of momentum and energy for a head on collision between a proton and an electron. Given the 90 MeV kinetic energy of the proton, the classical laws of mechanics can be applied and the maximum energy of the electron after collision is approximately 50 keV.

Figure 2 shows that the average proton energy decreases with depth and therefore the energy of the initial secondary electron will decrease with depth. However, the energy distribution of the secondary electrons is not dependent on the depth, as shown in figure 5. The reason is that a secondary electron will loose its energy by releasing many more electrons with lower energies. This results in a overall average energy of the secondary electrons of approximately 1.5 keV which is constant with depth. Such very low energy electrons deposit their energy almost instantaneously in tissue. Therefore only few electrons can travel far enough to cross the water–air interface. These electrons will return into the tissue by an arc-shaped trajectory with a 0.5 mm radius due to the Lorentz force. However, the relative contribution of these few electrons to the local energy deposition is very small. This explains why for proton irradiation in the presence of a magnetic field the electron return effect (ERE) is negligible. Also, because the energy distribution of the secondary electrons is independent on the proton energy the results will not change as function of the initial proton energy, except for the change of lateral shift as a function of the penetration depth as discussed above.

4.2. Hybrid MRI proton therapy system

As already mentioned in section 1, integrating MRI functionality with a proton therapy system faces serious technical hurdles. Basically, these are similar to those addressed for the technical feasibility work on integrating a 1.5 T MRI with a photon therapy system (Raaymakers *et al* 2004a, Lagendijk *et al* 2008):

- Interference by the magnetic field (B0) and the radiofrequency field (B1);
- Radiation delivery to the patient from outside MRI;
- Magnetic field induced dose effects within the patient.

For the hybrid MRI 6 MV photon therapy system we have chosen a design in which the 6 MV accelerator is positioned in a ring around a closed-bore 1.5 T MRI system. The MRI system is adjusted in order to minimize the magnetic interference and the beam absorption but still the beam travels through the equivalent of 10 cm aluminium. For a proton accelerator, similar modifications can be applied to minimize the magnetic interference. However, proton beam

transmission through any structure of a MRI system is not feasible. An open 0.5 T similar to the hybrid interventional MR/X-ray system by Fahrig *et al* (2001) seems more suitable. This approach will require a solution for the extended distance between the gantry and the patient. The radiofrequency interference can be solved by intermittent radiation and MRI acquisition at a millisecond timescale.

The magnetic field induced dose effects are minimal, as discussed above in section 4.1. An additional point of concern stems from the fact that the irradiation beam will also be deflected outside the patient due to the Lorentz force. The deflection depends on the magnetic stray field outside the MRI which will be lower than the nominal 0.5 T that is present in the bore of the magnet. The curvature of the proton beam will, therefore, be 2.8 m at the patient surface, while the beam will be much more straight near the gantry. The bending is in the transversal plane with respect to the patient and can be determined precisely using the magnetic stray field around the MRI; a small extra gantry rotation or translation can then correct for this effect.

Getting over the hardware challenges is the first step towards MRI guided proton therapy. Additional effort is required for the segmentation/tracking of target structures at MRI data in order to relate these to treatment planning data. Then automatic decision making is required to determine whether and how a treatment plan needs to be changed while taking the previous delivered dose into account. Finally, the dose distribution for the new plan and the updated anatomy has to be calculated and delivered. These issues are already under investigation in the context of image-guided radiotherapy (IGRT) using (conebeam) CT guidance (a.o. Smitsmans *et al* (2005), Lu *et al* (2006)) and for the real-time tracking of breathing related motion (f.i. Wijesooriya *et al* (2008)).

5. Conclusion

In contrast to photon therapy, the impact of a transverse 0.5 T magnetic field on the dose distribution for proton therapy is very small. At tissue–air interfaces no effect of the magnetic field on the dose distribution can be detected. This is due to the low energy of the secondary electrons released by the heavy protons. These conclusions are valid for all practical proton energies. Given the potential benefit of MRI guidance for proton therapy, these findings should serve as an encouragement for further investigation of the feasibility of a hybrid MRI proton therapy system.

References

Agostinelli S *et al* 2003 Geant4- a simulation toolkit *Nucl. Instrum. Methods Phys. Res.* A **506** 250–303

Allison J *et al* 2006 Geant4 developments and applications *IEEE Trans. Nucl. Sci.* **53** 270–8

Dawson L A and Sharpe M B 2006 Image-guided radiotherapy: rationale, benefits, and limitations *Lancet Oncol.* **7** 848–58

Fahrig R, Butts K, Rowlands J A, Saunders R, Stanton J, Stevens G M, Daniel B L, Wen Z, Ergun D L and Pelc N J 2001 A truly hybrid interventional mr/x-ray system: feasibility demonstration *J. Magn. Reson. Imaging* **13** 294–300

Greco C and Wolden S 2007 Current status of radiotherapy with proton and light ion beams *Cancer* **109** 1227–38

Kirkby C, Stanescu T, Rathee S, Carlone M, Murray B and G Fallone B 2008 Patient dosimetry for hybrid mri-radiotherapy systems *Med. Phys.* **35** 1019–27

Lagendijk J J W, Raaymakers B W, Raaijmakers A J E, Overweg J, Brown K J, Kerkhof E M, van der Put R W, Hårdemark B, van Vulpen M and van der Heide U A 2008 MRI /linac integration *Radiother. Oncol.* **86** 25–9

Lomax A J 2008 Intensity modulated proton therapy and its sensitivity to treatment uncertainties 2: the potential effects of inter-fraction and inter-field motions *Phys. Med. Biol.* **53** 1043–56

Lu W, Olivera G H, Chen Q, Ruchala K J, Haimerl J, Meeks S L, Langen K M and Kupelian P A 2006 Deformable registration of the planning image (kvct) and the daily images (mvct) for adaptive radiation therapy *Phys. Med. Biol.* **51** 4357–74

Raaijmakers A J E, Hårdemark B, Raaymakers B W, Raaijmakers C P J and Lagendijk J J W 2007a Dose optimization for the mri-accelerator: IMRT in the presence of a magnetic field *Phys. Med. Biol.* **52** 7045–54

Raaijmakers A J E, Raaymakers B W, Van der Meer S and Lagendijk J J W 2007b Integrating a mri scanner with a 6 MV radiotherapy accelerator: impact of the surface orientation on the entrance and exit dose due to the transverse magnetic field *Phys. Med. Biol.* **52** 929–39

Raaijmakers A J E, Raaymakers B W and W Lagendijk J J 2005 Integrating a MRI scanner with a 6 MV radiotherapy accelerator: dose increase at tissue–air interfaces in a lateral magnetic field due to returning electrons *Phys. Med. Biol.* **50** 1363–76

Raaijmakers A J E, Raaymakers B W and W Lagendijk J J 2008 Magnetic-field-induced dose effects in mr-guided radiotherapy systems: dependence on the magnetic field strength *Phys. Med. Biol.* **53** 909–23

Raaymakers B W, Lagendijk J J W, Van der Heide U A, Overweg J, Brown K, Topolnjak R, Dehnad H, Jurgenliemk-Schulz I M, Welleweerd J and Bakker C J G 2004a Integrating a MRI scanner with a radiotherapy accelerator: a new concept of precise on line radiotherapy guidance and treatment monitoring *The Use of Computers in Radiation Therapy* ed B Yong, S Do, E Kyung and W Sung (Seoul: ICCR Jeong Publishing) pp 89–92

Raaymakers B W, Raaijmakers A J E, Kotte A N T J, Jette D and Lagendijk J J W 2004b Integrating a MRI scanner with a 6 MV radiotherapy accelerator: dose deposition in a transverse magnetic field *Phys. Med. Biol.* **49** 4109–18

Schulz-Ertner D, Jäkel O and Schlegel W 2006 Radiation therapy with charged particles *Semin. Radiat. Oncol.* **16** 249–59

Smitsmans M H P, De Bois J, Sonke J J, Betgen A, Zijp L J, Jaffray D A, Lebesque J V and Van Herk M 2005 Automatic prostate localization on cone-beam CT scans for high precision image-guided radiotherapy *Int. J. Radiat. Oncol. Biol. Phys.* **63** 975–84

Unkelbach J, Chan T C Y and Bortfeld T 2007 Accounting for range uncertainties in the optimization of intensity modulated proton therapy *Phys. Med. Biol.* **52** 2755–73

Webb S 2001 *Intensity-modulated Radiation Therapy* (*Medical Sience Series*) (Bristol: Institute of Physics Publishing)

Wijesooriya K, Weiss E, Dill V, Dong L, Mohan R, Joshi S and Keall P J 2008 Quantifying the accuracy of automated structure segmentation in 4d ct images using a deformable image registration algorithm *Med. Phys.* **35** 1251–60